Department of Physics and Astronomy
University of Heidelberg

Bachelor Thesis in Physics
submitted by

Richard Naab

born in Wiesbaden (Germany)

2018

Prospects of searching for dark matter in the monophoton channel with the ATLAS detector.

This Bachelor Thesis has been carried out by Richard Naab at the
Kirchhoff-Institute for Physics in Heidelberg
under the supervision of
Prof. Dr. Hans-Christian Schultz-Coulon

Abstract

Dark matter is one of the most fundamentally unknown constituents of nature. It is observed up to the large scales that can be probed by astrophysical experiments, but its origin has not yet come to light.

The Large Hadron Collider (LHC) at CERN is - to this day - colliding particles at the highest energies and unprecedented luminosities, aiming at discovering the most fundamental properties of nature. The experiments at the LHC, amongst them ATLAS, therefore provide an interesting avenue to investigate the dark matter problem.

The goal of this study is to estimate the sensitivity of the ATLAS detector to possible dark matter candidates, described by simplified models. It analyzes events with one high energetic photon and associated missing transverse energy, at an integrated luminosity of $150 fb^{-1}$, which are expected to be collected by the end of 2018.

Zusammenfassung

Dunkle Materie stellt einen der am wenigsten bekannten Bausteine der Natur dar. Sie ist auf den größten Skalen beobachtet und mit astrophysikalischen Experimenten gemessen, der Ursprung bleibt jedoch bisher unbekannt.

Der Large Hadron Collider (LHC) am CERN untersucht Teilchenkollisionen höchster Energie und nie dagewesener Luminositäten, um die fundamentalen Eigenschaften der Materie zu verstehen. Die Experimente am LHC, zu welchen ATLAS gehört, bieten deshalb eine interessante Möglichkeit, das Problem der dunklen Materie zu untersuchen.

Ziel dieser Studie ist, die Sensitivität des ATLAS Detektors in Bezug auf mögliche Kandidaten dunkler Materie – beschrieben in simplified models – abzuschätzen. Untersucht werden Ereignisse mit einem hochenergetischen Photon und dazugehöriger fehlender transversaler Energie. Angenommen wird dabei eine integrierte Luminosität von $150 fb^{-1}$, welche voraussichtlich bis Ende 2018 erreicht wird.

Contents

Part I.
Introduction

This Bachelor thesis is structured as follows. In the first part, astrophysical and cosmological evidence for dark matter is presented. Subsequently, the concept of searches at particle colliders is derived. The strategy of the so called monophoton channel, looking for events with energetic photons and missing transverse energy, is discussed in detail.

The second part describes the experimental setup: The ATLAS detector, the use of Monte Carlo simulations to predict event yields for simplified models of dark matter as well as statistical methods employed in the analysis of these Monte Carlo samples.

Finally, the results of this study are presented in the third part, estimating the sensitivity of the monophoton channel at an integrated luminosity of $150 fb^{-1}$, which the LHC is expected to deliver until the end of Run 2 in 2018.

1. The dark matter problem

The standard model (SM) of particles presents a precise description of the fundamental interactions and elementary particles of nature. However, certain problems [1] cannot be explained within this theoretical framework. One of the shortcomings of the SM is that it does not include an explanation for the existence of dark matter (DM), which has been established by numerous astrophysical observations. Some of those are presented in the following. Zwicky [2] estimated the masses of galaxy clusters using the virial theorem. He found a large discrepancy between his calculations and the amount of observed luminous matter, leading him to speculations about a dark matter component. Later, the rotation curves of spiral galaxies were measured, beginning with the work of Rubin (see [3]). This yielded the astonishing result that at large distances from the galactic center, rotational velocities are much larger than expected from the directly observed luminous mass distribution. When introducing additional DM content within the galaxies, these curves could be explained as shown in Figure 1. Finally, DM is included in cosmological models to explain large scale structures of the universe [4]. These structures are quantified by measurements of photon radiation from the early universe, the cosmic microwave background, which provides the most precise constraints on the density of DM in the universe [5].

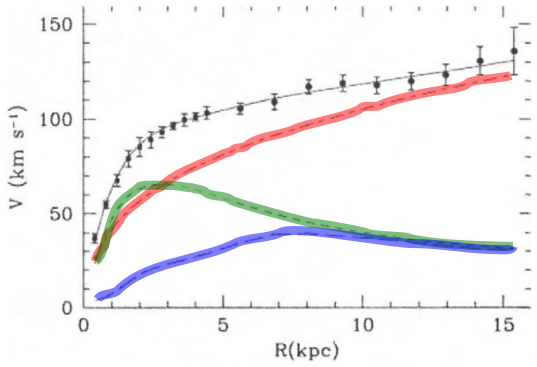

Figure 1: Velocities ν in a spiral galaxy as a function of the distance from the center. The data points are fit by the black line, which has contributions from dark matter (red), luminous matter (green) and gas (blue). Figure adopted from [4].

2. Collider searches for dark matter

In the currently most favored models aiming to explain the history of our universe, dark matter is described in terms of particles which are assumed to couple weakly to particles of the well known standard model of particle physics. Under this hypothesis, several search strategies can be established [6].

So called direct detection experiments aim at measuring the recoil of nuclei from collisions with dark matter particles coming from the local DM halo. In indirect detection experiments, resulting particles from DM annihilation are searched for. In a complementary way, collider searches are looking for the actual production of dark matter particles. One of the main advantages of this latter method is the fact that astrophysical uncertainties do not contribute to the measurements. This study presents one of these collider searches, which is detailed in the following.

An interaction of dark matter particles with the detector environment is very unlikely, otherwise one would already have observed dark matter directly or indirectly through radiation. Thus, the DM particles traverse the detector without being measured [7]. This leads to an energy and momentum imbalance in the transverse plane of such an event. This imbalance is quantified by the so called missing transverse energy $E_{T,miss}$, which is the norm of the vectorial sum of the momenta of all reconstructed particles in the plane orthogonal to the beamline.

Several analyses called "Mono-X" searches [8] aim at detecting events in which the production of dark matter particles is associated with $E_{T,miss}$ and another single object X of high transverse momentum. This object can be a jet, a photon, a W/Z or a higgs boson and recoils against the dark matter particles. This presents a distinct signature in

(a) Mono-jet (b) Mono-γ

Figure 2: Processes searched for by the mono-X analyses. Several interaction mechanisms (not specified here and represented by the grey circle) can be tested for.

which the Mono-X can be used to trigger on the pair production of DM.

The monophoton channel is the subject of this study, which has to compete with the monojet analysis. The latter presents the highest experimental sensitivity to the dark matter models considered [9]. The processes searched for in these two cases are shown in Figure 2. As discussed in chapter seven of [6], the cross section of the DM production in association with a gluon jet g, denoted $\sigma_{\chi\chi j}$, compares to the cross section of DM production with a photon $\sigma_{\chi\chi\gamma}$ as

$$\frac{\sigma_{\chi\chi\gamma}}{\sigma_{\chi\chi j}} \sim \frac{\alpha}{\alpha_s} \sim \frac{1}{15} \, . \tag{1}$$

Here, $\frac{\alpha}{\alpha_s}$ is the ratio of the electroweak and the strong coupling. It is derived in [6] that the significances obtained in the monophoton channel can compete with the monojet analysis in the following situations: When systematic uncertainties dominate the analyses or when there are high contributions of non-collision background in the monojet channel.

Part II.
Experimental setup and techniques

This chapter presents the methods used to analyze particle collisions in ATLAS. It includes the detector setup used to collect data, the simulation framework providing theoretical expectations and statistical methods used in the analysis of the data.

3. The ATLAS detector

ATLAS [10] is a multi-purpose detector situated at the CERN site near Geneva. It records proton-proton collisions from the Large Hadron Collider (LHC). The protons are accelerated with a chain of pre-accelerators to be finally injected clock- and anti-clockwise into the LHC, a storage ring of 27 km of circumference. Here they reach their nominal energy corresponding to a center-of-mass energy $\sqrt{s} = 13$ TeV and are brought to collision at designated crossing points, to be analyzed by several detectors: ALICE, ATLAS, LHCb and CMS.

The coordinate system used in ATLAS is centered at the nominal interaction point. The x-axis points to the center of the LHC, the y-axis points upwards and the z-axis of the right-handed system is oriented along the beam line. In the $x - y$ plane, cylindrical coordinates (r, ϕ) are used and one defines the pseudorapidity η as a function of the polar angle θ: $\eta = -\ln(tan\frac{\theta}{2})$.

The products of the collision in the center of ATLAS first traverse the so-called inner tracking detector (ID). High-granularity pixel and silicon microstrip trackers as well as a straw-tube transition radiation tracker cover a range of $|\eta| < 2.5$, aiming at precise momentum and vertex measurements. A superconducting solenoid surrounds the ID and provides a magnetic field of 2T to bend charged particles' trajectories, giving the possibility to discriminate them in direction, momentum and charge.

The detector's next layer consists of a lead and liquid argon sampling electromagnetic calorimeter (ECAL): In the lead an electromagnetic shower is induced. It is a cascade of electrons and positrons emitting Bremsstrahlung and photons undergoing pair-production. With longer distances traversed in the medium, the particle multiplicities grow and the energy of the individual particles decreases up to a point where low-energetic photons

and electrons are absorbed do not further propagate through the detector. The aim is then to measure as precisely as possible the energies of all particles in the shower in order to exactly reconstruct the incoming electron or photons energy. This measurement is performed in kapton electrodes which alternate with the lead plates and gaps of liquid argon in an accordion-shaped way over the full calorimeter coverage. This is shown in Figure 3. The electromagnetic shower ionizes the liquid argon. This ionization is read out in the kapton electrodes. The ECAL has a fine granularity in the central region matching the range of the ID, allowing for precision measurements of electrons and photons. This is also particularly interesting for this analysis.

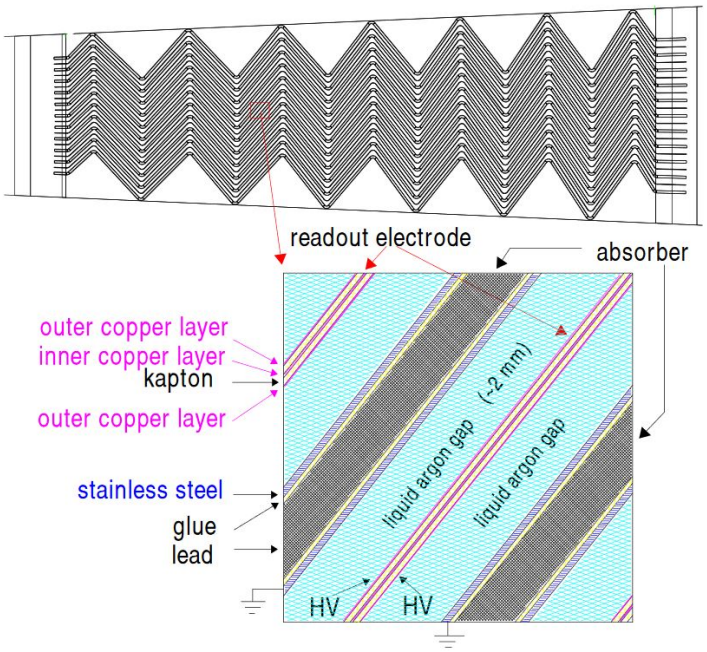

Figure 3: Schematic of the accordion-shaped ECAL, where the lower part details the alternating active and absorber layers. Figure taken from [11]

The surrounding hadronic calorimeter (HCAL) is following the same principles as its electromagnetic counterpart, aiming at measuring precisely the energy of hadrons created in the collisions. Those also produce showers when interacting with the detector. In this case they contain a larger number of different particles produced in strong interaction mechanisms. The HCAL is made of steel as absorber material and scintillator tiles in the active layer in the central region $|\eta| < 1.7$. Copper or tungsten in combination with liquid argon are used in the region $1.5 < |\eta| < 3.2$

The detector setup of ATLAS is completed by a muon system relying on the magnetic

field from superconducting toroid magnets. Those bend the muon trajectories so that the track information coming from the muon chambers can be used to extract their momenta. The muon chambers register the passage of charged particles either in drift tubes in the central region or cathode strip chambers at large η.

Recording event signatures from the proton-proton interactions is another technological challenge. The LHC delivers those collisions at a rate of 40 MHz, which is far too large to be stored for analyses. Therefore, a dedicated trigger system has been developed [12] to reduce the rate of events to be stored to a few hundred Hz. The so-called first level trigger evaluates detector information with reduced granularity for the full event rate of 40 Mhz. The aim is to identify events of possibly interesting signature and to reduce the incoming rate. Tracking information from the ID can only be taken into account within the high-level trigger (HLT). Since longer latencies are available at this stage, more complex software algorithms can be run so that the the HLT can process data selected by the fist level trigger. Finally, information from physics objects in the event are used in the HLT. Those objects are obtained through reconstruction algorithms: The detectors' outputs are digitized and all information from the ID, calorimeters and the muon system is used to identify particles produced in the collision.

4. Monte Carlo simulation

This section describes the techniques and methods used to obtain theoretical predictions for the outcome of the observed particle collisions. The essential question for searches like in the monophoton channel is the following: Is the observed number of events compatible with SM expectations or do we need extensions, as for example models of dark matter production, to describe the data correctly? In order to answer this question, one needs to calculate all possible contributions to a certain signature described within the given model. This is usually split into the two following steps. For a specific process, described by its Feynman diagram, first calculate the cross-section (representing the probability for this process to occur) and the four-momenta of all particles arising from the collision. Secondly, simulate the passage through the detector for all those particles in order to compare the theoretical prediction to the collected data. Both of these steps involve a large number of random choices (i.e.: Is there a photon emitted in the collisional process or not? When traversing the detector, is this photon disintegrating into a pair of e^+e^- at a given position $\vec{x}$?) where the random variables are distributed according to a certain probability density functions (pdf). This is treated by Monte Carlo (MC) methods, see e.g. [13].

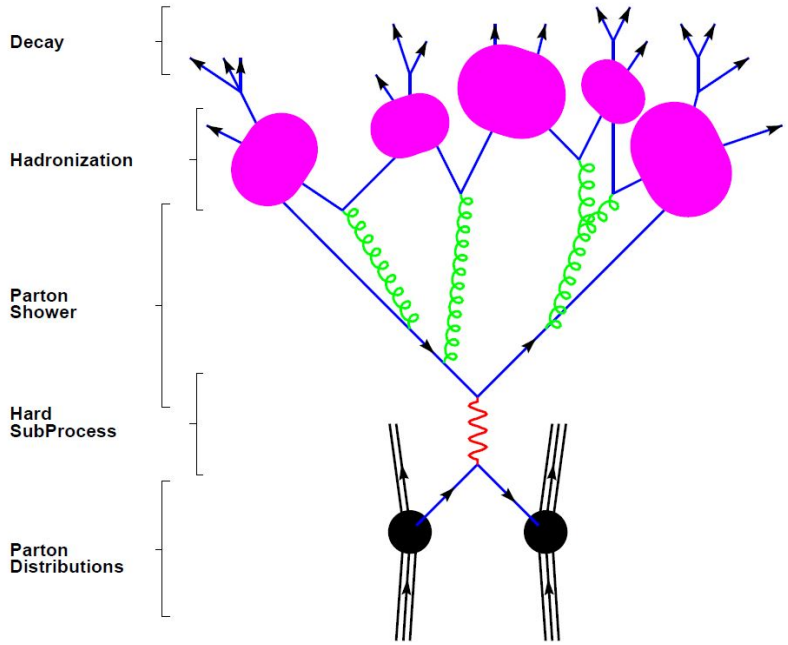

Figure 4: Schematic representation of the different stages of MC event generation evolving from the bottom to the top. Figure taken from [14]

The first of the above-mentioned steps is referred to as Monte Carlo generation of the event and it is summarized in Figure 4. The hard subprocess represents the Feynman diagram that is considered in the event and is evaluated by calculating the associated matrix element $\mathcal{M}_{hard\,subprocess}$. In order to determine the outgoing particles' four-momenta one also needs to know the momenta of the incoming particles (which can be quarks or gluons, both referred to as partons, forming the substructure of the colliding protons). These are described by the so-called parton density functions. The outgoing particles of the hard subprocess can ba accompanied by radiation of supplementary particles, which play a major role in QCD and are referred to as parton showers. According to the theory of strongly interacting particles, those partons then hadronize to form mesons and baryons as bound states. Finally, since some of the involved particles may have a very short lifetime, there can be decays of those particles before they interact with the detector. At this final stage of MC event generation events are stored in a so-called "truth" format. This represents all outgoing particles and kinematic distributions coming from the generation only.

All particles of such an event are then propagated through the virtual ATLAS detector, which is implemented in the software framework GEANT4 [15]. All detector subsystems,

like the ID, the calorimeters and the muon system are included in the simulation in order to obtain a detector outputs equivalent to that coming from real particle collisions in ATLAS. Also, the effect of other collisions occurring at the same time, known as pileup effect, is included. This virtual output is then treated by exactly the same algorithms for reconstruction so that simulated events and actual data feature an identical data structure.

Note that this simulation demands a lot of CPU resources, and the simulation of the calorimeters demands a large percentage of simulation time. Therefore, there also exist so-called "fast" simulations algorithms that approximate the "full" GEANT4 approach by directly replacing low-energetic electromagnetic particles by shower shapes obtained from full simulation of the calorimeters [16].

5. Statistical interpretation

This section gives an overview of the statistical methods used for interpreting the results. A central concept is the construction of so-called "signal" and "control" regions ("SR" and "CR"). The former corresponds to selection of cuts in phase space aiming for a high contribution from the signal. The latter represents a region in phase space where the signal has very low contributions whereas one or more specific background processes have an enhanced contribution.

The CRs are used to verify and further constrain the background information coming from MC generation: By fitting the MC expectation to the actual data, one extracts so-called k-factors, describing the normalization of a MC sample given this comparison between theory and data. The MC samples considered at this stage usually represent certain hard processes contributing to the final signature.

In order to obtain the final background estimation, one constructs a likelihood function as following: The event yield in a certain CR α is described by a Poisson pdf ($pois$) with mean

$$N_{CR^\alpha} = k_{(p\,1)} N^\alpha_{(p\,1)} + k_{(p\,2)} N^\alpha_{(p\,2)} + k_{(p\,3)} N^\alpha_{(p\,3)} + .. \tag{2}$$

where $N_{(p\,X)}$ is the MC expectation for process X in that region and $k_{(p\,X)}$ is the associated normalization factor. Systematic uncertainties relevant in this region are considered as so-called nuisance parameters (NP). They are considered to be distributed according to a gaussian pdf ($gauss$), their uncertainties represented by the width of the associated

Gaussian pdf. The final likelihood function reads:

$$L = \prod_{CRs} \left(pois(N_{CR}) \times \prod_{NPs(CR)} gauss(NP) \right) \tag{3}$$

and has all the k-factors and the NPs as free parameters to be adjusted by maximizing L. This procedure is called background-only fit [17].

When including a signal sample - for example from a dark matter model - one also considers the SRs in the likelihood function. For one signal region β with a predicted number of signal events N^{β}_{sig} from MC, the mean of the Poisson pdf is

$$N_{SR^{\beta}} = \mu N^{\beta}_{sig} + \sum_{pX} k_{(p\,X)} N^{\beta}_{(p\,X)} \ , \tag{4}$$

where μ defines the so called signal strength, that can be varied in order to test different hypotheses (see below) [18]. In such a case with a signal sample included, the likelihood function is defined as:

$$L = \prod_{SRs} \left(pois(N_{SR}) \times \prod_{NPs(SR)} gauss(NP) \right) \times \prod_{CRs} \left(pois(N_{CR}) \times \prod_{NPs(CR)} gauss(NP) \right) \tag{5}$$

The question then arising from this comparison is to what extend the observed event yield is compatible with a background-only hypothesis b or whether an additional signal hypothesis $s + b$ has to be considered in order to describe the event yield correctly. To discriminate between those two hypothesis one constructs a test statistic denoted q, following a certain pdf $f(q|H)$ given a hypothesis H. Suppose the choice of q leads to the pdfs $f(q|s + b)$ and $f(q|b)$ as shown in Figure 5. One then defines the so-called p-values

$$p_{s+b} = P(q \geq q_{obs}|s + b) = \int_{q_{obs}}^{\infty} f(q|s + b))dq \tag{6}$$

$$p_s = P(q \leq q_{obs}|s) = \int_{-\infty}^{q_{obs}} f(q|s))dq \ . \tag{7}$$

Those are the probabilities for a repeated experiment to obtain a result of q that is less or at most equally in agreement with the hypotheses than it is the observed value q_{obs}. Take for example an experiment yielding $p_{s+b} = 5\%$, one would then reject the $s + b$ hypothesis at a 95% "confidence level" (CL).

This choice of p_{s+b} can be misleading when the signal that is looked at has a very low yield in comparison to the background hypothesis. The curves $f(q|s + b)$ and $f(q|b)$ from Figure 5 then would be very close to each other so that large values of p_b would imply

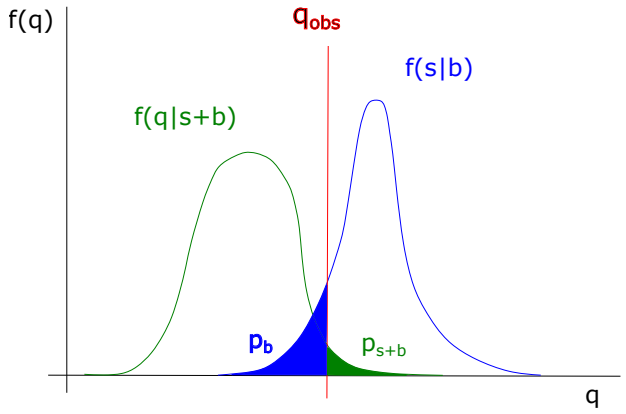

Figure 5: Schematic explaining the definition of the p-values

low values of p_{s+b}. If the number of background events had some statistical downward fluctuation leading to a large p_b, one would consider the $s+b$ to be very unlikely and exclude the signal. The test therefore has in principle no sensitivity to this signal. It is therefore common to use the modified CL_s technique which defines

$$p_s = \frac{p_{s+b}}{1-p_b} \tag{8}$$

as well as the associated

$$CL_s = 1 - p_s \tag{9}$$

This takes the described problem into account: CL_s will be much smaller than CL_{s+b} in cases where the signal is very low compared to the background and $1-p_b$ is small for low values of p_{s+b} [19].

Common test statistics used for analyses like the monophoton analysis include the so called profile likelihood ratio, which is defined as [20]:

$$\lambda(\mu) = \frac{L(\mu, \hat{\hat{\theta}})}{L(\hat{\mu}, \hat{\theta})} \tag{10}$$

Here, θ denotes the set of remaining parameters in the likelihood, that are the k-factors as well as the NP and μ is treated as a varying parameter as mentioned above. $\hat{\mu}$ and $\hat{\theta}$ are the values that globally maximize L and $\hat{\hat{\theta}}$ is the value maximizing L for a given μ.

The test statistic q is then defined as

$$q = -2 \ln \lambda(\mu) \tag{11}$$

with varying refinements in cases where only $\mu \geq 0$ is considered or $\mu = 0$ is set as a hypothesis for discovering a new signal. In general, large values of q correspond to cases where $L(\mu, \hat{\hat{\theta}})$ is small. When setting limits on the signal strength, these low values of the likelihood function for a given μ are interpreted as low compatibility of the hypothesized value of μ with the actual observation.

Part III.
Data analysis

The aim of this part is to describe the studies performed on Monte Carlo samples for the main background processes as well as for dark matter signals obtained from a so called simplified model. These are analyzed in order to obtain a final estimate of ATLAS' sensitivity to such a DM signal assuming an integrated luminosity of $\mathcal{L}_{int} = 150 fb^{-1}$.

6. Search strategy

In this section, the main aspects of the 2017 paper on the monophoton channel [21], which is the starting point for this study, are presented.

A first step in the analysis chain is the definition of "candidate" physics objects, which refer to the interpretation of the hits obtained in the different sub-detectors. Photons are expected to leave a trace only in the electromagnetic calorimeter, the candidate γs are therefore obtained from clusters of energy deposits in the ECAL. If the clusters do not correspond to an associated track, the candidate is considered as a unconverted photon. If there is an associated track, converted photons can be distinguished from electrons which leave a similar signature, mainly based on the information of conversion vertices as described in [22]. In any case, information about the trajectory is obtained from the segmentation in the calorimeters, in the case of converted photons information from the ID is used in addition. The profile of the energy deposits in the ECAL is used to identify photons and candidate objects are required to have a transverse energy $E_T^{\gamma} > 10$GeV, correspond to the "loose" identification criteria [23] and be within $|\eta| < 2.37$. Candidate electrons are reconstructed similarly to photons by using tracking information also and they are required to have $p_T^e > 7$GeV as well as $|\eta^e| < 2.47$. Candidate muons are obtained by combining tracks from the MS and the ID. They are required to have $p_T^{\mu} > 6$GeV and $|\eta^{\mu}| < 2.7$. Candidate jets are obtained from clusters of energy deposits in the calorimeters [24] and reconstructed using the anti-k_t algorithm with a radius parameter $R = 0.4$, more information can be found in [21]. The requirements on the jet kinematics in the event selection are $p_T^{jet} > 30$GeV and $|\eta^{jet}| < 4.5$. Based on all these candidate objects, one can finally define the missing transverse energy $E_{T,miss} = \sqrt{(E_x^{miss})^2 + (E_y^{miss})^2}$, where the two components orthogonal to the beam are:

$$E_{x(y)}^{miss} = E_{x(y)}^{miss,e} + E_{x(y)}^{miss,\gamma} + E_{x(y)}^{miss,\mu} + E_{x(y)}^{miss,jets} + E_{x(y)}^{miss,SoftTerm} \tag{12}$$

Each summand is the negative vectorial sum of the momenta from all reconstructed objects:

$$E_{x(y)}^{miss,object} = -\sum p_{x(y)}^{object} \tag{13}$$

and $E_{x(y)}^{miss,SoftTerm}$ refers to tracks from the primary vertex which are not associated with any of the listed objects (see [25] for details on the reconstruction algorithm of $E_{T,miss}$). To avoid double counting of energy deposits in the calorimeters, the objects are calibrated as in the order given in formula (12).

Having defined the physics objects arising from the *pp*-collisions, one can then apply selection criteria, aiming at high signal acceptances and simultaneously low background contaminations. The trigger applied for the analysis requires $E_T^\gamma > 140$GeV and the photon candidate to fulfill "loose" ID requirements. A primary reconstructed vertex is required and events with bad-quality photons or jets are removed, see [22] and [26].

The signal regions correspond to the different bins in $E_{T,miss}$, which are treated as exclusive bins. In those SRs, the leading photon is defined as the one with the highest p_T^γ in each event and is asked to have $E_T^\gamma > 150$GeV. An additional requirement for the photon is $|\eta| < 1.37$ or $1.52 < |\eta| < 2.37$ corresponding to the coverage of the ECAL and it has to fulfill "tight" ID criteria. The photon also has to be isolated (this corresponds to an upper cut on the energy deposits around photon's cluster baricenter in a cone $\Delta R = \sqrt{(\Delta\eta)^2 + (\Delta\phi)^2} = 0.4$) and to have $|z| < 0.25$m, where z is the distance between the beamspot and the crossing of the photon trajectory with the beamline. This latter cut rejects beam background with muons leaving a fake photon signature in the ECAL. A further cut $\frac{E_{T,miss}}{\sqrt{\sum E_T}} > 8.5$ GeV$^{\frac{1}{2}}$, with $\sum E_T$ being the scalar sum of all transverse momentum from the reconstructed objects that approximately describes the resolution of $E_{T,miss}$ (see [27]), is applied. In order to suppress events with poorly reconstructed jets faking $E_{T,miss}$, only 0 or 1 jet are accepted in the events and the azimuthal separation between the jet and the missing transverse energy, $\Delta\phi(jets, E_{T,miss})$, has to be greater than 0.4. Finally, events containing at least one electron or one muon are rejected in order to suppress background events from leptonically decaying W/Z bosons.

The reconstruction algorithms for the different objects above and other effects induce systematic uncertainties in the final estimate of the signal yield. The complete list of those systematics can be found in [21], the most important contributions in the analysis considering $\mathcal{L}_{int} = 36.1 fb^{-1}$ of data arise from the rate of fake photons from jets (ranging from 1.3% to 5.3% depending on the SR) and due to uncertainties in the jet energy scale (ranging from 1.4% to 5.6%). These are however dominated by statistical uncertainties varying from 6.1% to 14% depending on the signal region considered. This is the main

motivation for this study: With an increased integrated luminosity the accumulated statistics reduces those uncertainties, so that one expects a higher sensitivity to DM signals.

7. Background estimation

7.1. Background processes and control regions

As described in the previous analysis of the monophoton channel in the ATLAS detector, corresponding to $\mathcal{L}_{int} = 36.1 fb^{-1}$, there are several standard model processes (referred to as "background" in the following) yielding events of the same signature as the monophoton process (Figure 2b):

- Processes containing one photon of high E_T and neutrinos (ν) cannot be distinguished from a monophoton signature since neutrinos pass the ATLAS detector without detection. Therefore, electroweak events $Z(\rightarrow \nu\bar{\nu}) + \gamma$ with a Z boson decaying to two neutrinos represent a main background contribution

- The monophoton signature can be mimicked by processes yielding a γ and additional leptonic or hadronic particles: In $W(\rightarrow \nu l) + \gamma$ or $Z(\rightarrow l\bar{l}) + \gamma$ events, the electrons or muons (denoted by the "l") can be missed by the reconstruction algorithm. Similarly, $jets + \gamma$ events can contribute when the jets are mismeasured in the detector and thus imitate $E_{T,miss}$.

- Finally, either electrons or jets can be misidentified as photons in the ECAL and therefore possibly yield a monophoton signature. These are called "fake photons" and mainly originate from W/Z+jets, diboson, or multijet events.

In order to estimate the contribution of processes with true photons (the first two items in above's list), non-overlapping Monte Carlo samples have been generated and passed through the detector simulation. The event yield N from processes of a certain cross section σ is given by

$$N = \mathcal{L} \times \sigma \ , \tag{14}$$

where $\mathcal{L}$ denotes the corresponding luminosity. This gives the scaling to the new luminosity to be applied to the background data samples.

The MC event yields from the different background sources are verified by including several control regions (see Section 5). Three leptonic control regions, containing either one electron ("1eCR"), one muon ("1μCR") or two muons ("2μCR"), are defined to

constrain the W/Z backgrounds. The cuts applied are the same as in the SRs, except that the veto on leptons is inverted to increase the background contribution in this region. The muon or electron term is then dropped in the computation of $E_{T,miss}$ (formula 12), so that the leptons are treated as non-interacting particles. The condition containing $\sum E_T$ is also not applied.

Finally, a control region is defined to constrain background events containing photons and jets ("PhJetCR"). For this region, 85GeV$< E_{T,miss} <$ 110GeV and $\Delta\phi(\gamma, E_{T,miss}) <$ 3.0 are required.

7.2. Adapted binning and fake photons

Given these tunings one can now look at the total background yield in the different regions. Due to the increased luminosity the statistical error on the bin contents decreases: Since the relative statistical error scales as $\sim \frac{1}{\sqrt{N}}$ (N being number of events), one expects and observes a scaling of $\sqrt{\frac{36.1fb^{-1}}{150fb^{-1}}}$ for these errors. This can then be used to modify the binning of the signal and control regions. The hypothesized dark matter signal is expected to be distinguishable from SM background especially at higher missing transverse energy, searching in bins of high $E_{T,miss}$ is therefore preferred. A finer binning also helps distinguishing between DM signals and background by the shape of their $E_{T,miss}$-distributions.

Having this in mind, it was studied how the increased statistics would permit to redefine the binning in the signal and control regions. Aiming for bin contents and associated uncertainties comparable to the 2017 analysis, it was found that an added fourth bin was in agreement with this objective. Table 1 represents the three regions mainly concerned for such a comparison, the 1μCR and PhJetCR contain a much larger number of events and therefore do not limit the statistical uncertainty. The table also clearly shows that a possibly added fifth bin would not contain enough events to satisfy the proposed criteria.

The impact of events with fake photons is evaluated by means of data driven techniques. But since by the time this study was performed the full dataset had not yet been collected, an extrapolation is needed in order to measure the contribution of fake photons. The event yield in the different bins of the signal and control regions, as presented by the 2017 paper [21], is scaled to the new luminosity and then fitted with an exponential function to be able to estimate the number of fake photons in bins of higher missing transverse energy. The functional form is justified by the expectation that the background contribution should decrease exponentially with growing $E_{T,miss}$. Note that in this case, the last bin is an inclusive bin, containing all events above $E_{T,miss} =$ 300GeV. Adding more bins,

Table 1: Comparison of different binning configurations: The second column represents bin contents of the last bin from the 2017 analysis. The third and fourth columns represent bin contents of the last bin for possible configurations of added bins. All are treated as inclusive bins.

lower limit of last bin (corresponding $\mathcal{L}_{int}$)	**300 GeV** ($36.1 fb^{-1}$)	**375 GeV** ($150 fb^{-1}$)	**450 GeV** ($150 fb^{-1}$)
events in SR	226 ± 18	344 ± 14	141 ± 6
events in 2μCR	21.0 ± 2.0	28.6 ± 4.3	12.1 ± 4.2
events in 2eCR	18.0 ± 2.0	22.4 ± 1.6	5.8 ± 0.9

which is the goal of this extrapolation, leads to an overestimation of the content of these new bins since the third bin then should only contain events up to a certain upper bin limit. The chosen approach represents a conservative estimate since one overestimates the background contribution and therefore is less sensitive to some potential dark matter signal. This comes from the third bin because it should contain less events, and also from the added bins since the slope will be less steep with an overestimated third bin. However, the fake photon events make up less than 5% of the total background in the added bin. Therefore only a small fraction is concerned by this estimation.

Finally one could then obtain the total background estimation for this configuration, which is presented in Figure 6. These event yields of all relevant SM processes will be compared to hypothetical dark matter signals in the following section.

8. Estimates based on MC generation

The aim of this section is to present some first estimates based on the generation of dark matter signals. As done in the previous analysis, an axial-vector interaction in the simplified model is being investigated. This model is a benchmark model for dark matter searches as described by the joint ATLAS/CMS dark matter forum [7]. It includes DM particles as well as a mediator particle, which is defined to couple to SM particles as well as DM particles. Following the recommendations formulated in [28], the coupling of the quarks to the mediator particle is set to $g_q = 0.25$ and the coupling of the dark matter particles to the mediator is set to $g_\chi = 1$. The remaining free parameters in the generation are the masses of the dark matter particle (m_χ) and the mediator (M_{med}). Figure 7 shows the process to be simulated, presenting the mentioned parameters as well. The dark matter simplified model MC signal samples are generated with MadGraph [29].

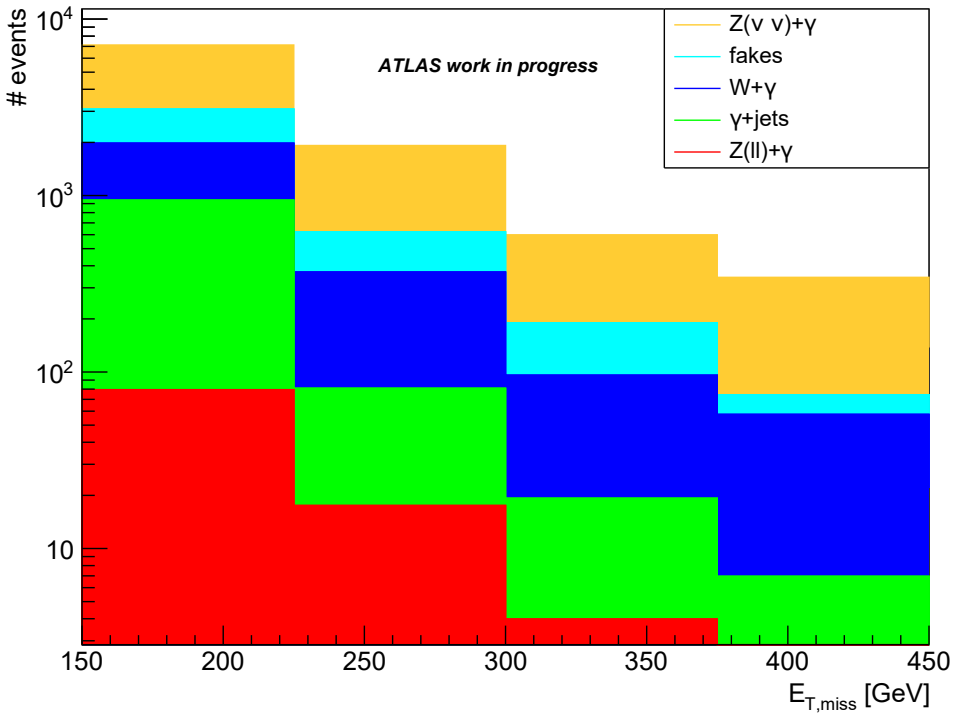

Figure 6: Background contribution in the signal region at $\mathcal{L}_{int} = 150 fb^{-1}$

Pythia [30] is used for showering. Note that a filter $E_T^{\gamma} > 130$GeV is used in order to avoid generating events which are not of interest.

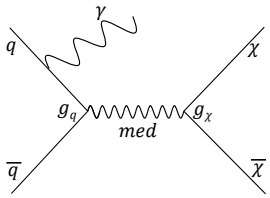

Figure 7: Mono γ process in a simplified model interaction.

To probe the two-dimensional mass plane, a few mass points with a fixed value of $m_{\chi} = 10$GeV and values increasing from $M_{med} = 1200$GeV were generated to extend the existing grid of simulated mass points. This strategy was chosen as a starting point since the exclusion limit in M_{med} at very low m_{χ} is one of the characteristics of the typical exclusion plots [9]. An important note to make is that for these and all other samples

generated for this analysis, full detector reconstruction was not available due to its high consumption of CPU time. Instead, event information at truth level was used: Data from MC event generation that is usually passed to detector simulation can also be processed to extract all particles and their kinematic distributions before interaction with the detector (see Section 4). This is to be treated carefully since the truth objects do not correspond to physics objects that are actually reconstructed. The following Section 9 treats this problem in more detail and gives an estimation of the detector effects missing to the events analyzed at truth level.

The approximation which is to follow however relies on truth information, combined with an averaged detector efficiency that was calculated in the 2017 analysis. The ROOT framework [31] provides data handlers to process this truth data, so that event yields in the signal region can be estimated. Figure 8 shows the acceptance as function of the mediator mass for different cuts. The acceptance A describes the ratio of events passing cuts at truth level to the total number of generated events

$$A = \frac{N_{cuts,truth}}{N_{generation,total}} \ . \tag{15}$$

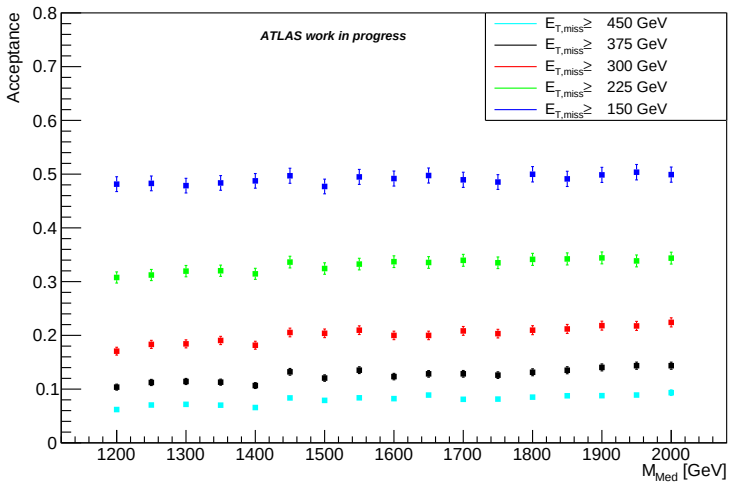

Figure 8: Acceptance for fixed m_χ, where the cuts are applied as described in the text together with a threshold in $E_{T,miss}$

One observes that with the cut at $E_{T,miss} = 150$GeV the acceptance remains constant for all mediator masses, whereas cuts of higher $E_{T,miss}$ lead to slightly increasing A with higher M_{med}. This is due to the fact that the pair production of $\chi\bar{\chi}$ with a heavier

mediator shifts the event's distributions to higher missing transverse energy.

To finally estimate the event yield of such a DM signal one needs to take into account the effects of the detector. From the 2017 analysis, the so called efficiency ϵ was extracted, which describes the percentage of events coming from the stage of cuts on truth level that also pass reconstruction

$$\epsilon = \frac{N_{reconstructed}}{N_{cuts,truth}} \tag{16}$$

so that the product $A \times \epsilon$ describes the total percentage of generated events that pass all cuts. Thus, equation 14 now reads

$$N = \mathcal{L} \times \sigma \times A \times \epsilon \ . \tag{17}$$

These numbers ϵ were calculated per reconstructed point in the (M_{med}, m_χ) plane, where the highest mass available was $M_{med} = 1200\text{GeV}$. Since this is the point closest to the generated models of higher mediator masses, its efficiency was applied to those of higher M_{med} under the approximation that the detector effects vary little.

Finally, the signal yield in the different SR (corresponding to different bins in $E_{T,miss}$) could be compared to the total background estimation. This was done by calculating the significance for both exclusive and inclusive bin scenarios: It is given by the number of signal events divided by the square root of the number of background events per bin considered

$$s = \frac{N_{signal}}{\sqrt{N_{background}}} \ . \tag{18}$$

This assumes that the number of background events is gaussian distributed with standard deviation $\sqrt{N}$. The significance thus describes the excess of events with respect to background expectation in multiples of the standard deviation.

Figure 9 presents those calculations, clearly showing that the bin of highest $E_{T,miss}$ gives the highest discrimination between signal and background. Commonly, exclusion limit are set at 2σ, which corresponds to a 95% confidence level. This means that the probability of a real signal covered by background fluctuations is less than or equal to 5%. Figure 9 indicates that exclusion limits of this analysis could reach up to mediator masses of $1700 - 1800\text{GeV}$.

An important remark is that this result based on the significances does not include the following aspects: Firstly systematic uncertainties were not yet considered in this estimate. Those increase the total uncertainty on the background estimation, which augments the probability for a signal to hide in background fluctuations. Secondly, this estimate did not include the control regions. The CRs help constraining the background processes

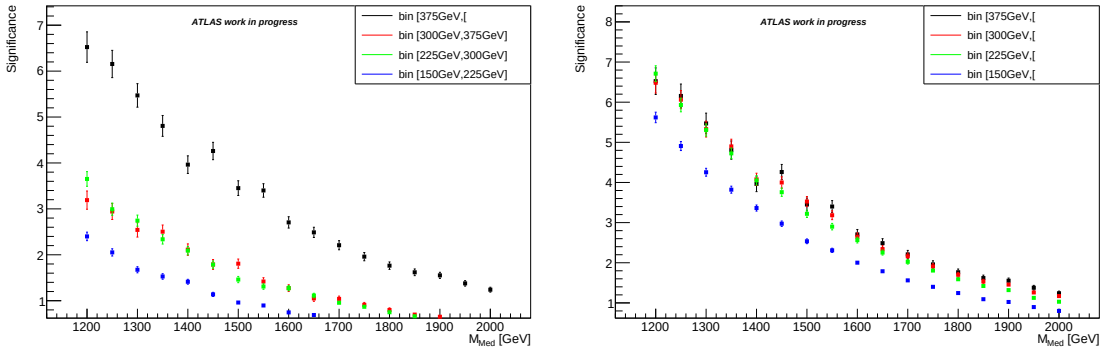

(a) exclusive bins

(b) inclusive bins

Figure 9: Significance for fixed $m_\chi = 10GeV$ and varying M_{med}.

which can reduce the uncertainty on their event yields.

9. Reweighting MC samples

This section describes the estimation of detector effects by the technique of reweighting of histograms. This uses truth information from MC generation. Whenever a range of model parameters are tested against the background predictions (as in the case of the monophoton analysis, the (M_{med}, m_χ) plane is scanned), the number of model points representing different parameterizations in a specific model can be large and therefore full detector reconstruction becomes too costly in terms of computing resources. In such cases, methods to inter- or extrapolate the existing grid of model points are helpful to refine predictions made in a specific model.

9.1. Description of the method

The reweighting method relies on the fact that essentially the detector simulation and event reconstruction do not depend on the model input used for MC event generation, since the software used for these steps is the same. The goal therefore is to estimate a transfer function T describing those detector related effects in a universal (model independent) way. Figure 10 shows the effect this transfer function can have on a showcase kinematic distribution. Note that the transfer function also is unitary, i.e. every truth level event is transformed to a reconstructed one (even though it may not pass cuts applied at this final stage). As described in [32], T can be extracted if there is one model point for which a fully reconstructed sample exists. This sample then probes the transfer function up to

a certain precision related to the finite sample size.

When generating different model points, the kinematic distributions may change. For example, $E_{T,miss}$, p_T^γ or η^γ vary with modified masses of mediator and dark matter particles involved in this process. This is described in theory by parameter dependent matrix elements $\mathcal{M}$ (a function of $(E_{T,miss}, p_T^\gamma, \eta^\gamma)$ for example) describing the possibilities for an event corresponding to a specific point in phase space to occur. Differences in $\mathcal{M}$ can be compared at generator level, so that the idea is to extract those differences based on truth information and then use the transfer function to obtain the detector output for the events of a new model point.

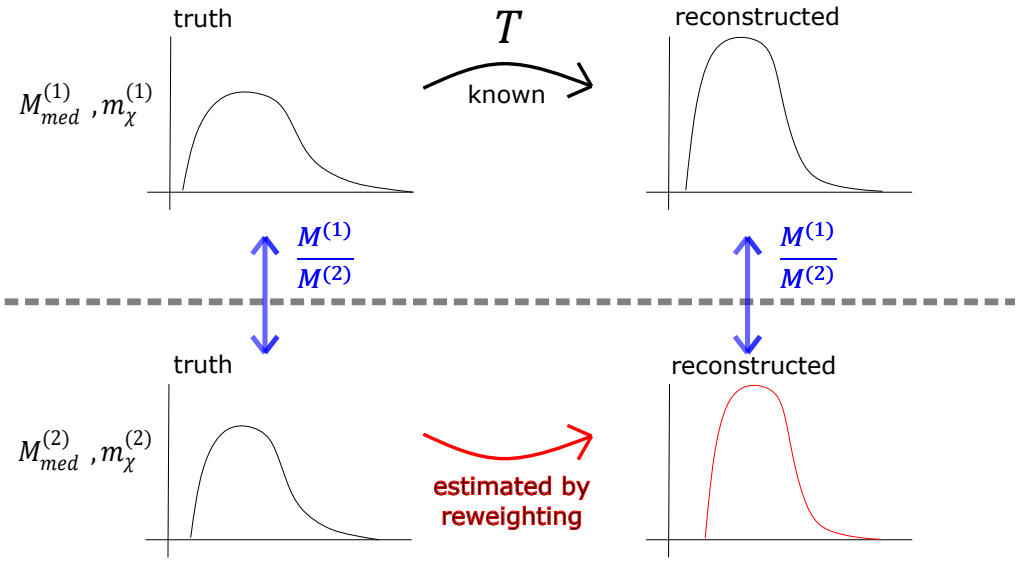

Figure 10: Scheme of the reweighting method. Two model points $M_{med}^{(1)}, m_\chi^1$ and $M_{med}^{(2)}, m_\chi^2$ are shown with their showcase distributions of a kinematic variable. The weights are given by the ratios of the matrix elements $\frac{\mathcal{M}^{(1)}}{\mathcal{M}^{(2)}}$.

In the limit of large statistics, when the concerned region of phase space is sufficiently probed, the matrix elements become proportional to the number of events in a corresponding bin of phase space, taking into account its necessary discretization through binning in the concerned variables. The method can then be reduced to calculating ratios of bin contents of histograms describing the main discriminating kinematic distributions. These ratios are then applied on the reconstructed sample event by event to obtain the

estimated detector effects for the model to be reweighted.

9.2. Validation using MC samples

The approach chosen in this analysis was to reweight the events based on truth information of the missing transverse energy solely. The reason is that multi-dimensional reweighting demands large sample sizes in order to provide sufficient statistics in the individual bin contents. It was found that $E_{T,miss}$ permits good discrimination between the samples. The "reference" or "base" model point with respect to which the ratios were calculated was chosen such as to be as close as possible in the (M_{med}, m_χ) plane to the model point to be reweighted (called "target" model point in the following).

To validate the method, reweighted samples were compared to their reconstructed equivalent. The target model points chosen for validation therefore corresponded to the reconstructed samples that were available. Those samples were taken from the group's work on the previous analysis and an important remark is that the events in those samples already had cuts applied: An event cleaning required an associated vertex, and events containing jets of high p_T which are compatible with noise in calorimeters. These are expected to have almost no impact on the sample. The subsequent cuts required the event to pass the trigger and have $p_T^\gamma > 125\text{GeV}$, good η^γ and $E_{T,miss}^{no\,e,no\,\mu} > 70\text{GeV}$. This removed $\mathcal{O}(5\%)$ of the events from the samples, depending on the corresponding M_{med} and m_χ.

A first validation was made where the weights

$$w(E_{T,miss}^{truth}) = \frac{n_{target}(E_{T,miss}^{truth})}{n_{base}(E_{T,miss}^{truth})} \tag{19}$$

were calculated based on the truth information coming from the reconstructed samples directly. Here $n_{target/base}(E_{T,miss}^{truth})$ denotes the histogram entries for a given bin. This yielded a good agreement, showing that the method works well when using the correct truth information (see Figure 15 in the appendix). Since, as described above, the distributions of $E_{T,miss}^{truth}$ were already cut on, the approach was modified for application to model points of higher masses M_{med} and m_χ: The distributions of $E_{T,miss}^{truth}$ were taken from newly generated samples both for the target model *and* the base model, so that two homogeneous distributions without any cuts were compared. The result of this method is shown in Figure 11. The plot compares the number of events per final bin in the signal region obtained from reweighting with the event yield from the reconstructed sample. A more detailed comparison is shown in Figure 16 in the appendix. The reweighted

distribution shows less agreement than obtained with the previous method, which was further examined: A possible shortcoming is that the truth information used for the base model is incorrect, since it comes from the own newly generated samples - these are not the events that are actually reconstructed so that there is a disagreement. However, in the limit of high numbers of generated events the distributions from different MC generations should converge to the same ones, and it was checked with samples of high event numbers as well as samples with different random seeds that the final disagreement between reconstruction and reweighting was not an issue of limited statistics. Also, it was tried to mimic the cuts applied on the reconstructed samples at truth level, which did not give a better result either. A final remark is that the statistical errors on the weights $w(E_{T,miss}^{truth})$ was of $\mathcal{O}(1\%)$, slightly depending on the binning. This considerably below the statistical error coming from the MC generation itself. Also, various binning options of $E_{T,miss}^{truth}$ were tested, all giving the same result within statistical uncertainty.

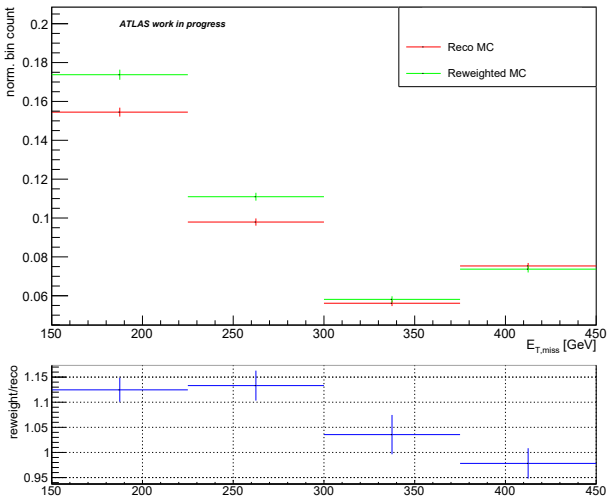

Figure 11: Validation of the reweighting method that uses truth information from the self produced MC samples, as described in the text. The base model (M_{med} = 1100GeV, m_χ = 10GeV) and the target model (M_{med} = 1200GeV, m_χ = 10GeV) were used.

The further analysis still relies on the reweighting, since one needs to estimate the detector effects on the MC generation. The observed disagreement ranging up to $\sim 10\%$ in certain bins has to be taken into account as an uncertainty on the signal yield of the reweighted models. It shows as an uncertainty on the signal strength μ, which is studied in the following section. The efficiencies resulting from this method are then

obtained by comparing the number of events after cuts on the reweighted samples with the acceptances resulting from the generation (see Figure 14 in the appendix). Figure 17 shows the obtained efficiencies in the plane of M_{med} and m_χ.

10. Expected exclusion limits

This section presents the main results of this study: The ATLAS detector's estimated sensitivity with respect to a simplified dark matter model in the monophoton channel assuming data from collisions corresponding to $\mathcal{L}_{int} = 150fb^{-1}$. Since this study is based on simulated MC samples only, one cannot directly compare MC background expectations to actually observed signal yields. The approach therefore is to assume the MC background expectation to be correct and to compare those to model points of simplified dark matter models. Different values of the parameters m_χ and M_{med} are scanned. For each of those model points, CL_s is probed to be able to interpolate to a line in the (M_{med}, m_χ) plane describing the expected exclusion at a confidence level of 95%.

10.1. Software setup

The software used to obtain a MC background estimation based on the definition of the signal and control regions and to subsequently perform the hypothesis tests for different model points is HistFitter [17]. It incorporates certain key elements, such as the CR and SR concepts, an efficient treatment of systematic errors and an automated procedure to obtain the likelihood functions. It is based on the ROOT analysis framework [31], which provides data structure, functions for plotting and fitting algorithms that were also used in the sections above. The setup of HistFitter for this analysis includes the definition of the different SRs and CRs by specifying the respective cuts which are described in Section 6. Also, the different background processes and the signal models to be considered are set: Either by providing the MC samples, stored as ROOT trees, or by directly creating histograms for a specific process. The former technique was applied for the $Z(\nu\nu)\gamma$, $W\gamma$, γjets and $Z(ll)\gamma$ backgrounds using the generated MC samples as in Section 7, the latter for the background of fake γ's, using the extrapolation of the data-driven estimation from the 2017 analysis as described in Section 7. The signal samples obtained from the reweighting method (Section 9) were also stored as ROOT trees, allowing a treatment of the DM models analogous to the previous monophoton analysis.

The systematic uncertainties related to the reconstruction of the physics objects are treated by varying the respective parameter by $\pm 1\sigma$ and keeping separately stored trees for those up- or downward fluctuations. HistFitter then extracts the effect of this variation

on the signal yield by comparing to the result from the nominal tree. This methods permits to easily integrate the variation of the signal regions based on cuts on $E_{T,miss}$, since both steps of applying the cuts and evaluating the systematic uncertainties based on the trees are done by the program. Other systematics coming from data-driven estimates are given directly as an input to the HistFitter software. Those related to statistical precision (as for the fake γ's) are scaled by $\frac{1}{\sqrt{N}}$ accounting for the increased luminosity with respect to the previous analysis. There is a systematic uncertainty describing the extrapolation from the γ+jets CR to the SRs. This systematic uncertainty needs to be estimated for the fourth bin as well. It was set to equal the uncertainty of the first bin, corresponding to the maximal value found in all bins, which is a conservative approach.

Based on this setup, the background estimation can also be obtained in HistFitter, which in comparison to Section 8 also includes the control regions. In order to do so, a background-only fit (see Section 5) is performed. Since this study relies on samples from MC simulation only, all the regions are "blinded" in the fit, meaning that the MC expectation before the fit is assumed to be correct and no comparison to data is made [17]. This leads to k-factors (which describe the normalization of the MC samples obtained from the comparison to data) all equal to unity. But still, the fit provides constraints on the background processes since the uncertainty on the number of events arises from the k-factors instead of the $\sqrt{N}$ width of the assumed Poisson distribution for a simple counting experiment. The decrease in statistical uncertainty is observed to be $\mathcal{O}(0,5\%)$ depending on the SR. The results of the background-only fit are presented in Table 2. This table extends the event yields presented in Figure 6 firstly by the uncertainties now coming from the fitting procedure and secondly by the event yields in the different CRs.

The event yields of the different background processes can then be compared to dark matter signals of the axial-vector simplified model interaction. The corresponding reweighted MC samples are given as input to the HistFitter software which extracts the expected number of events in the SRs by applying the cuts as described above. The systematic uncertainties are evaluated by reading ROOT trees of up- and downward variations for the parameters concerned. To compare this study to the results of the searches [9], so-called exclusion fits are then performed for various tuples (M_{med}, m_χ) to obtain upper limits. These are set on the signal strength μ, which is an additional multiplicative factor considered for the signal sample's event yield (see equation 4). The condition $\mu \geq 0$ is set since the dark matter models considered are not expected to decrease the total signal yield.

Figure 12 shows the result of the hypothesis tests for one specific set of parameters, where a range of values of μ are tested. The different CL are presented for comparison,

Table 2: MC background estimation resulting from the fit for $\mathcal{L}_{int} = 150fb^{-1}$. The total fitted background is shown, as well as the contibutions from the different background processes. The definition of the SRs and CRs can be found in the text. The PhJetCR is common for all four SRs.

	SR1	SR2	SR3	SR4
Fitted Background	7100 ± 110	1921 ± 48	599 ± 22	344 ± 18
$Z(\to \nu\nu)\gamma$	4040 ± 220	1299 ± 53	409 ± 38	270 ± 20
$W(\to l\nu)\gamma$	1038 ± 61	288 ± 24	77 ± 11	50.6 ± 7.0
$Z(\to ll)\gamma$	79.4 ± 5.0	17.5 ± 1.1	3.98 ± 0.50	2.11 ± 0.22
γ + jets	860 ± 180	63 ± 51	16 ± 16	4.8 ± 3.5
Fake γ's from electons	630 ± 110	141 ± 32	54 ± 13	6.0 ± 1.5
Fake γ's from jets	448 ± 57	112 ± 22	40 ± 32	10.8 ± 5.1
Fitted 1μCR	2901 ± 57	922 ± 30	285 ± 17	183 ± 14
Fitted 2μCR	622 ± 20	214 ± 17	65.4 ± 5.6	29.3 ± 4.5
Fitted 2eleCR	513 ± 20	168.2 ± 8.2	53.9 ± 5.1	22.9 ± 2.3
Fitted PhJetCR	19750 ± 630	19750 ± 630	19750 ± 630	19750 ± 630

it becomes visible that CL_s generally has larger values than CL_{s+b}, according to the definition in equation 9. The green and yellow band show the 1σ and 2σ variations of the observed curve for CL_s. In this case where the MC expectation is assumed to be true, the "expected" and "observed" curves are identical, normally the expected curve refers to the MC estimation and the observed curve corresponds to the comparison with real data. Finally note that the value of CL_b equals 0.5 for every point tested, which is also due to the fact of assuming the MC expectation to be correct. In a case where data would strictly equal the background prediction, one has no means of rejecting or not rejecting the CL_b hypothesis since one has to assign a probability of 50% to it.

10.2. Exclusion lines in the (M_{med}, m_χ) plane

Finally putting all this together, one can extract exclusion lines in the two-dimensional parameter space of (M_{med} and m_χ). These are obtained by performing tests as shown in Figure 12 for a large number of parameter couples, each time registering the value of μ corresponding to $CL_s = 95\%$. These values are than plotted in the (M_{med}, m_χ) plane, which is automatically filled with interpolated values by the ROOT plotting algorithms. The final estimated of the expected sensitivity is then taken as the line representing an

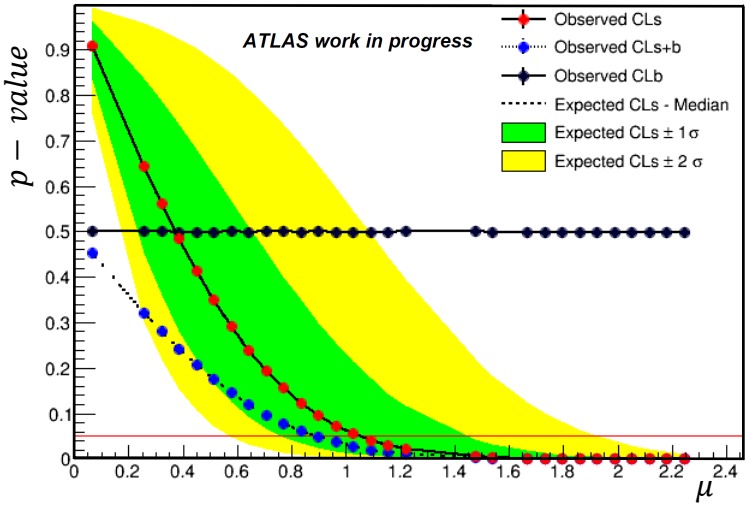

Figure 12: Example of the hypotheses tested for the model point $M_{med} = 1200$ GeV, $m_\chi = 300$ GeV with varying signal strength μ. The dots represent the values of μ which were tested for, the horizontal red line shows where the different CL reach 95 %

exclusion of μ equal to unity at a 95% CL. The scan value $\mu = 1$ simply means that the DM signal sample is not further modified, so that the couples (M_{med}, m_χ) on the exclusion line are excluded at 95% CL with their nominal cross-section. An exclusion at 95% CL set for smaller μ can be interpreted in the way that the model point in question would be excluded even if the corresponding cross-section was scaled down by a factor μ and the signal yield therefore was lower. Similarly, an exclusion of $\mu > 1$ means that the cross-section of the model point would have to be a factor μ higher in order to possibly be excluded. The resulting plot is shown in Figure 13. One can see that the exclusion limit reaches up to about $M_{med} = 1300$GeV for low masses of the DM particle. Coming closer to the diagonal where $M_{med} = 2m_\chi$ the exclusion limit then goes back as the cross-section of the generation rapidly drops near this diagonal that separates the lower right regime where the dark matter particles are produced on-shell and the upper left regime where they are produced off-shell. The $\pm 1\sigma$ lines are obtained by plotting the same contour map as shown in the plot, in this case not with the nominal values of the excluded μ but with those corresponding to the up- and down-variation of the excluded signal strength by 1σ. One observes that the $\sim 10\%$ uncertainty on μ coming from the reweighting method (Section 9) is well within the band of the $\pm 1\sigma$ uncertainty coming from the fit. Finally, the results from the preceding analysis [21] on the monophoton channel are shown for

comparison.

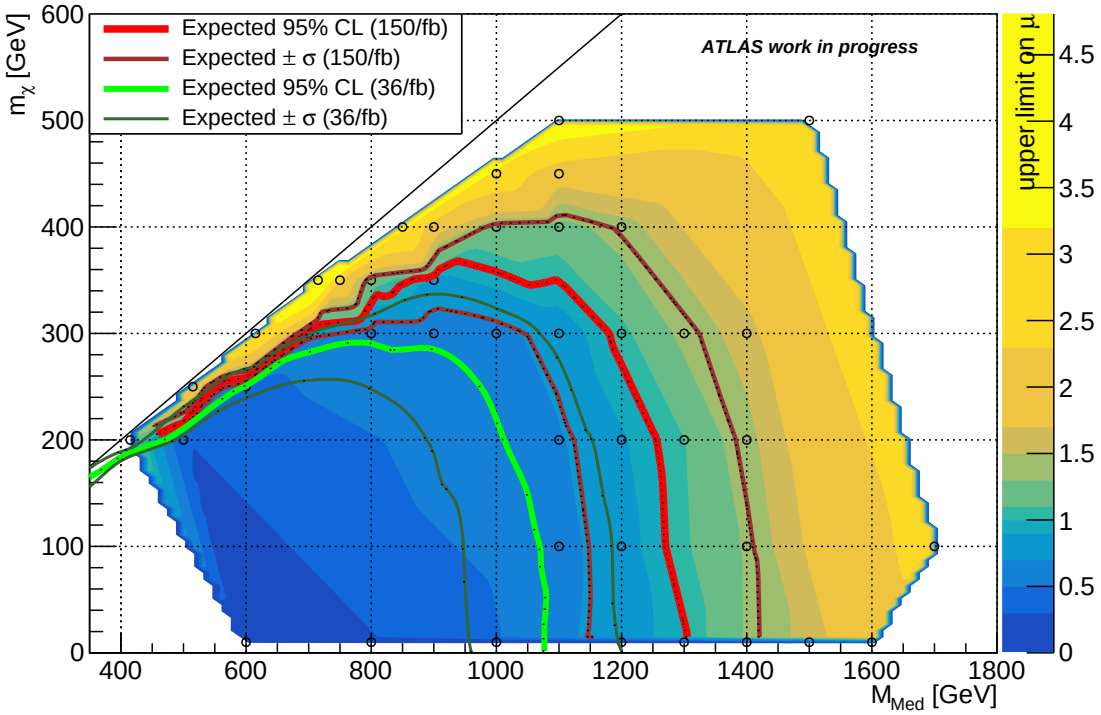

Figure 13: Signal strengths μ excluded at 95% CL in the (M_{med}, m_χ) plane. The black circles represent the points that were explicitly tested. The exclusion line, obtained as explained in the text, resulting from this study is shown in red. The green line is the exclusion line from the 2017 paper, corresponding to an analysis with $\mathcal{L}_{int} = 36fb^{-1}$ of data.

This result contrasts the estimates made in Section 8 where limits at around $M_{med} =$ 1700GeV were expected. Since the background estimation used to obtain the limits were the same in both cases, this difference comes from the uncertainties in the fit. These are shown in Table 3. The contribution of the individual uncertainties are evaluated by setting the parameter in question constant, then fitting again and calculating the quadratic difference of this fit and the default result from the original fit. The systematics correspond to the uncertainties in the reconstruction of the objects discussed above. One can see that the uncertainties become large in the SRs of high $E_{T,miss}$, where limited statistics come from both the SRs itself as well as the corresponding CRs.

Furthermore, the limits were compared to the cross sections of the signal generation in the (M_{med}, m_χ) plane, see Figure 18 in the appendix. It was observed that the

Table 3: Post-fit uncertainties in the different signal regions evaluated in HistFitter. The individual contributions do not necessarily add in quadrature since they can be correlated. The sources of the different systematic uncertainties are detailed in [21].

	SR1	SR2	SR3	SR4
Total uncertainty	2.4%	4.4%	8.8%	15.4%
Statistical uncertainty	2.0%	3.9%	7.1%	13.3%
Systematic uncertainty	1.1%	2.2%	4.2%	6.1%
Resolution of e and γ	0.2%	0.2%	0.5%	0.9%
Scale of e and γ	0.3%	0.6%	0.3%	0.4%
Jet energy resolution	0.2%	0.2%	1.0%	2.9%
Jet energy scale	0.6%	0.5%	0.9%	2.9%
Fake e	1.8%	1.7%	2.1%	1.8%
Fake jets	0.7%	0.9%	1.5%	2.0%
Resolution of $E_{T.miss}$	0.1%	<0.1%	0.6%	0.4%
Scale of $E_{T.miss}$	0.1%	0.5%	0.5%	0.2%
Pileup effects	0.4%	2.0%	1.5%	0.6%

exclusion line followed approximately a line of constant cross section, in agreement with the observation that the kinematic distributions do not change significantly with varying M_{med} or m_χ. The cross section corresponding to the process therefore is a significant variable when setting limits on these simplified models of dark matter.

Following the discussion in Section 2, the obtained limits were also compared to the exclusion lines originating from the analysis of the monojet channel [33] (Figure 19 in the appendix). Even though only $\mathcal{L}_{int} = 36fb^{-1}$ of data are analyzed the obtained limits are higher than those resulting from this study: For low masses of the dark matter particle, mediator masses higher than $M_{med} = 1800$GeV are excluded in the monojet analysis. This search can profit from theory calculations that permit to also extensively use CRs with W-bosons to estimate the main $Z(\rightarrow \nu\nu)$+jet BG. The monophoton analysis, in contrast, uses the CRs with Z-bosons for the estimation of the main $Z(\rightarrow \nu\nu) + \gamma$ BG. Since the production rate is approximately ten times higher for W-bosons, this increases the number of events in the CRs helping to constrain the background estimation.

To finally evaluate the impact of different choices of the signal regions (i.e. the defined binning in $E_{T,miss}$), the fit was re-run with various options as presented in Table 4, showing the exemplary limits obtained for one model point. The results were obtained in

Table 4: Comparison of different SR configurations for performing the HistFitter limits for the model point $M_{med} = 1400$GeV, $m_\chi = 200$GeV, only statistical uncertainties are treated. The first option refers to this study, the second to the 2017 analysis. The third and fourth option are cases where the lower bins in $E_{T,miss}$ are split into two distinct SR. The last options represent single inclusive SR.

choice of SR	$\mu_{limit}^{expected}$	$\mu_{limit}^{exp.+1\sigma}$	$\mu_{limit}^{exp.-1\sigma}$
4 SR	1.007	0.732	1.386
3 SR	0.976	0.707	1.346
split SR2	0.972	0.704	1.341
split SR1 & SR2	0.969	0.702	1.337
1 SR: $E_{T,miss} \geq 300$GeV	1.123	0.817	1.543
1 SR: $E_{T,miss} \geq 150$GeV	2.272	1.616	3.224

fits including only statistical uncertainties, as only relative differences in the limits set on μ are of interest and those are not expected to change significantly when the systematics are fully considered. The table shows that a configuration with 3 SR could have yielded slightly more stringent limits than obtained with the 4 SR chosen for this study. The advantage of a fourth bin of higher missing transverse energy in which the signal sample can in principle be more easily distinguished from background as observed in Section 8 is constrained by higher systematic and statistic uncertainties in this fourth bin. Tests were made for configurations in which those were split into two separate SR and no bin of high $E_{T,miss}$ was added. This is based on the fact that SR1 and SR2 provide large statistics and could be split up, the cut was made in order to obtain two new signal regions with equal number of events. Finally, configurations with one inclusive SR were chosen, showing that the most stringent limits indeed come from SR of high $E_{T,miss}$.

11. Conclusion and Outlook

In this study, the sensitivity of the monophoton channel to a dark matter simplified model was predicted by assuming $\mathcal{L}_{int} = 150 fb^{-1}$ of collected data. By using the same search strategy as the previous analysis of $\mathcal{L}_{int} = 36 fb^{-1}$, the expected limits on the model parameters increased. Those limits help constraining dark matter models and improving the understanding of its origin.

The result was obtained from the analysis of Monte Carlo samples of the axial-vector simplified model. This included the method of histogram reweighting to estimate detector effects. Those dark matter signal samples were compared to background predictions from Monte Carlo as well as estimated contributions from fake photon events. Hypothesis tests using the CL_{s+b} technique yielded upper limits on the signal strength μ of the dark matter signals. Those upper limits in the two-dimensional parameter space gave the expected line below which simplified models are excluded at 95% confidence level.

Despite higher statistics in the prediction, a main limitation comes from low event yields in signal regions of high $E_{T,miss}$. For low values m_χ, limits on M_{med} increased from 1100 GeV (corresponding to $\mathcal{L}_{int} = 36 fb^{-1}$) to approximately 1300 GeV ($\mathcal{L}_{int} = 150 fb^{-1}$).

The monojet channel, which used the signature of a single jet rather than a single photon, still provides more stringent limits than this study. However, the monophoton channel provides a complementary approach, which can also be interesting when combining the results from both analyses.

The reweighting method used to avoid costly simulation of the detector response can be interesting for each analysis relying on generated models of varying parameters. A desirable approach would be to validate the method by using fast calorimeter simulation (FastSim) to reconstruct Monte Carlo for a certain set of model parameters.

An enhancement the analyses in the monophoton channel could profit from are theoretical calculations that permit to use Monte Carlo samples with W-boson instead of such with Z-bosons. These computations also includes the shape of backgrounds with W- and Z-bosons as a function of $E_{T,miss}$. By using these, an analysis can profit from a single k-factor for one sample instead of independent k-factors per individual bin in the signal region. This helps increasing the statistics in the control regions.

References

[1] S. Troitsky. *Unsolved problems in particle physics*. 2011. arXiv: 1112.4515.

[2] F. Zwicky. "Die Rotverschiebung von extragalaktischen Nebeln". In: *Helvetica Physica Acta* 6 (1933), pp. 110–127.

[3] G. Bertone and D. Hooper. *A History of Dark Matter*. 2016. arXiv: 1605.04909v2.

[4] S. Dodelson. *Modern Cosmology*. Academic Press, 2003. ISBN: 978-0-12-219141-1.

[5] Planck Collaboration. *Planck 2015 results. XI. CMB power spectra, likelihoods, and robustness of parameters*. 2015. arXiv: 1507.02704.

[6] T. Plehn. *Yet Another Introduction to Dark Matter*. 2017. arXiv: 1705.01987.

[7] D. Abercrombie et al. *Dark Matter Benchmark Models for Early LHC Run-2 Searches: Report of the ATLAS/CMS Dark Matter Forum*. 2015. arXiv: 1507.00966.

[8] F. Kahlhoefer. *Review of LHC Dark Matter Searches*. 2017. arXiv: 1702.02430.

[9] The ATLAS Collaboration. *Summary plots from the ATLAS Exotic physics group*. 2018. URL: https://atlas.web.cern.ch/Atlas/GROUPS/PHYSICS/CombinedSummaryPlots/EXOTICS/ (visited on 09/04/2018).

[10] The ATLAS Collaboration. "The ATLAS Experiment at the CERN Large Hadron Collider". In: *Journal of Instrumentation* 3.08 (Aug. 2008). ISSN: 1748-0221.

[11] N. Ilic. "Performance of the ATLAS Liquid Argon Calorimeter after three years of LHC operation and plans for a future upgrade". In: *Journal of Instrumentation* 9.3 (2014). ISSN: 17480221. arXiv: 1306.6756v2.

[12] F. Pastore. "The ATLAS Trigger System: Past, Present and Future". In: *Nuclear and Particle Physics Proceedings* 273-275 (2016), pp. 1065–1071. ISSN: 24056014.

[13] G Cowan. *Statistical Data Analysis*. Oxford science publications. Clarendon Press, 1998. ISBN: 9780198501558.

[14] M. A. Dobbs et al. *Les Houches Guidebook to Monte Carlo Generators for Hadron Collider Physics*. 2004. arXiv: 0403045 [hep-ph].

[15] S. Agostinelli et al. "Geant4—a simulation toolkit". In: *Nuclear Instruments and Methods in Physics Research Section A: Accelerators, Spectrometers, Detectors and Associated Equipment* 506.3 (July 2003), pp. 250–303. ISSN: 0168-9002.

[16] The ATLAS Collaboration. *The ATLAS Simulation Infrastructure*. 2010. arXiv: 1005.4568.

[17] M. Baak et al. "HistFitter software framework for statistical data analysis". In: *The European Physical Journal C* 75.4 (2015), p. 153. ISSN: 1434-6044. arXiv: 1410.1280.

[18] M. Wu. "Search for Dark Matter and Supersymmetry in the single photon events with the ATLAS detector". PhD thesis. Université Grenoble Alpes, 2015.

[19] A. Read. "Presentation of search results: the CL s technique". In: *Journal of Physics G: Nuclear and Particle Physics* 28.10 (2002), pp. 2693–2704. ISSN: 0954-3899.

[20] G. Cowan et al. "Asymptotic formulae for likelihood-based tests of new physics". In: *European Physical Journal C* 71.2 (2011). ISSN: 14346052. arXiv: 1007.1727.

[21] ATLAS Collaboration. "Search for dark matter at \sqrt{s}=13TeV in final states containing an energetic photon and large missing transverse momentum with the ATLAS detector". In: *European Physical Journal C* 77.6 (2017). ISSN: 14346052. arXiv: arXiv:1704.03848v2.

[22] The ATLAS Collaboration. *Expected photon performance in the ATLAS experiment*. Tech. rep. ATL-PHYS-PUB-2011-007. Geneva: CERN, Apr. 2011. URL: https://cds.cern.ch/record/1345329.

[23] The ATLAS Collaboration. "Measurement of the photon identification efficiencies with the ATLAS detector using LHC Run-1 data". In: *European Physical Journal C* 76.12 (2016). ISSN: 14346052.

[24] The ATLAS Collaboration. "Topological cell clustering in the ATLAS calorimeters and its performance in LHC Run 1". In: *European Physical Journal C* 77.7 (2017). arXiv: arXiv:1603.02934v3.

[25] The ATLAS Collaboration. "Performance of algorithms that reconstruct missing transverse momentum in \sqrt{s} = 8 TeV proton–proton collisions in the ATLAS detector". In: *European Physical Journal C* 77.4 (2017). arXiv: arXiv:1609.09324v2.

[26] The ATLAS Collaboration. *Selection of jets produced in proton-proton collisions with the ATLAS detector using 2011 data*. Tech. rep. ATLAS-CONF-2012-020. Geneva: CERN, 2012. URL: https://cds.cern.ch/record/1430034.

[27] The ATLAS Collaboration. *Performance of missing transverse momentum reconstruction in proton-proton collisions at 7 TeV with ATLAS*. Aug. 2011. arXiv: 1108.5602. (Visited on 09/04/2018).

[28] A. Boveia et al. *Recommendations on presenting LHC searches for missing transverse energy signals using simplified s-channel models of dark matter*. 2016. arXiv: 1603.04156.

[29] J Alwall et al. “The automated computation of tree-level and next-to-leading order differential cross sections, and their matching to parton shower simulations”. In: *Journal of High Energy Physics* 2014.7 (2014), p. 79. ISSN: 1029-8479.

[30] T. Sjöstrand, S. Mrenna, and P. Skands. “A brief introduction to PYTHIA 8.1”. In: *Computer Physics Communications* 178.11 (2008), pp. 852–867. ISSN: 0010-4655.

[31] I. Antcheva et al. *ROOT - A C++ Framework for Petabyte Data Storage, Statistical Analysis and Visualization*. 2015. arXiv: 1508.07749.

[32] J. Gainer et al. “Exploring theory space with Monte Carlo reweighting”. In: *Journal of High Energy Physics* 2014.10 (2014), pp. 1–12. ISSN: 10298479. arXiv: 1404.7129.

[33] ATLAS Collaboration. *Search for new phenomena in final states with an energetic jet and large missing transverse momentum in pp collisions at \sqrt{s}=13 TeV using the ATLAS detector*. 2016. arXiv: 1604.07773.

A. Additional plots

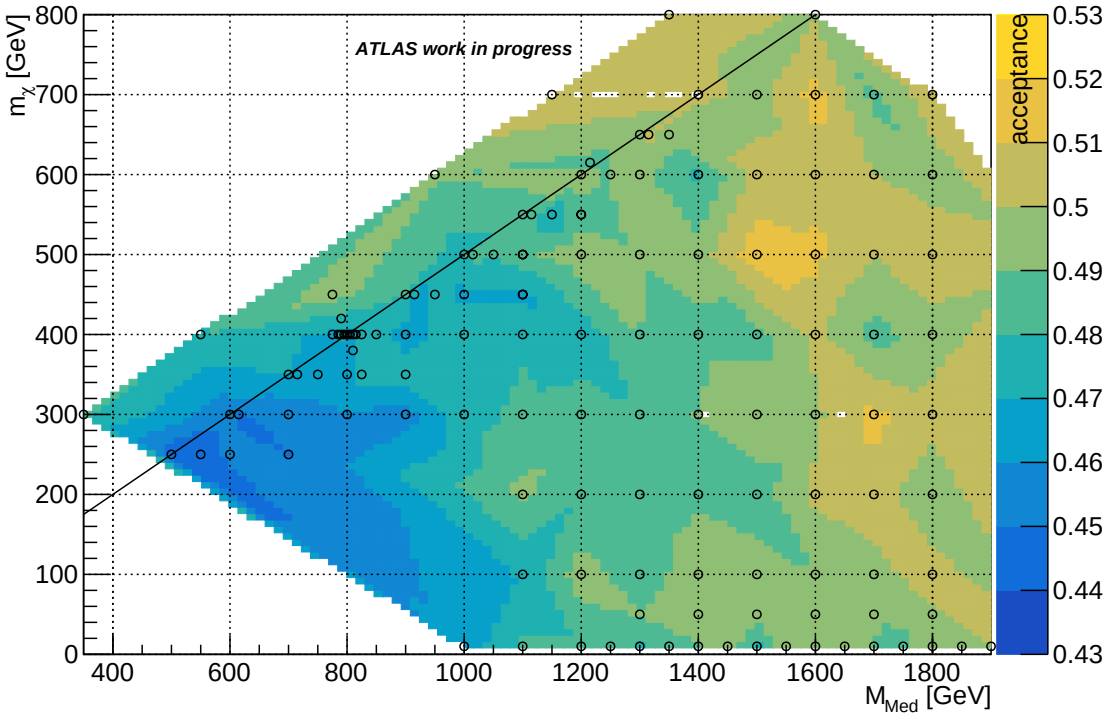

Figure 14: Acceptances from the generation of dark matter simplified model signals (section 8). The black dots represent couples of the parameters M_{med} and m_χ that were generated.

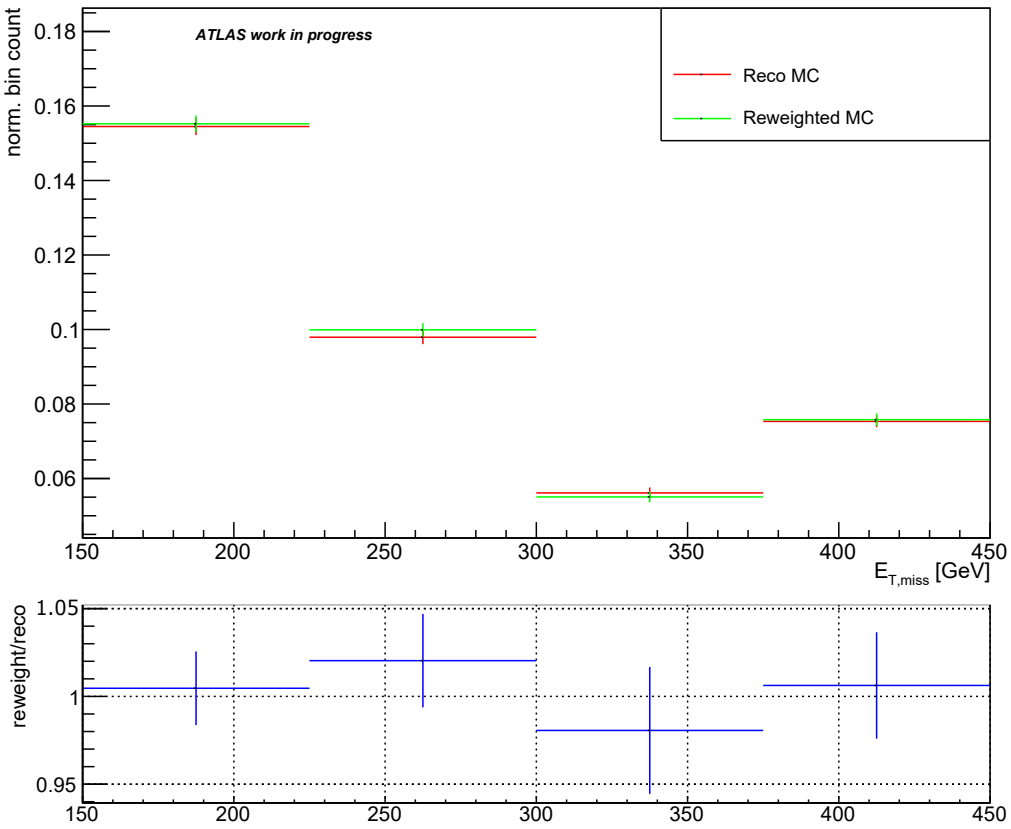

Figure 15: Validation of the reweighting method that uses truth information from the reconstructed MC samples, as described in the text of Section 9. The base model ($M_{med} = 1100$GeV, $m_\chi = 10$GeV) and the target model ($M_{med} = 1200$GeV, $m_\chi = 10$GeV) were used.

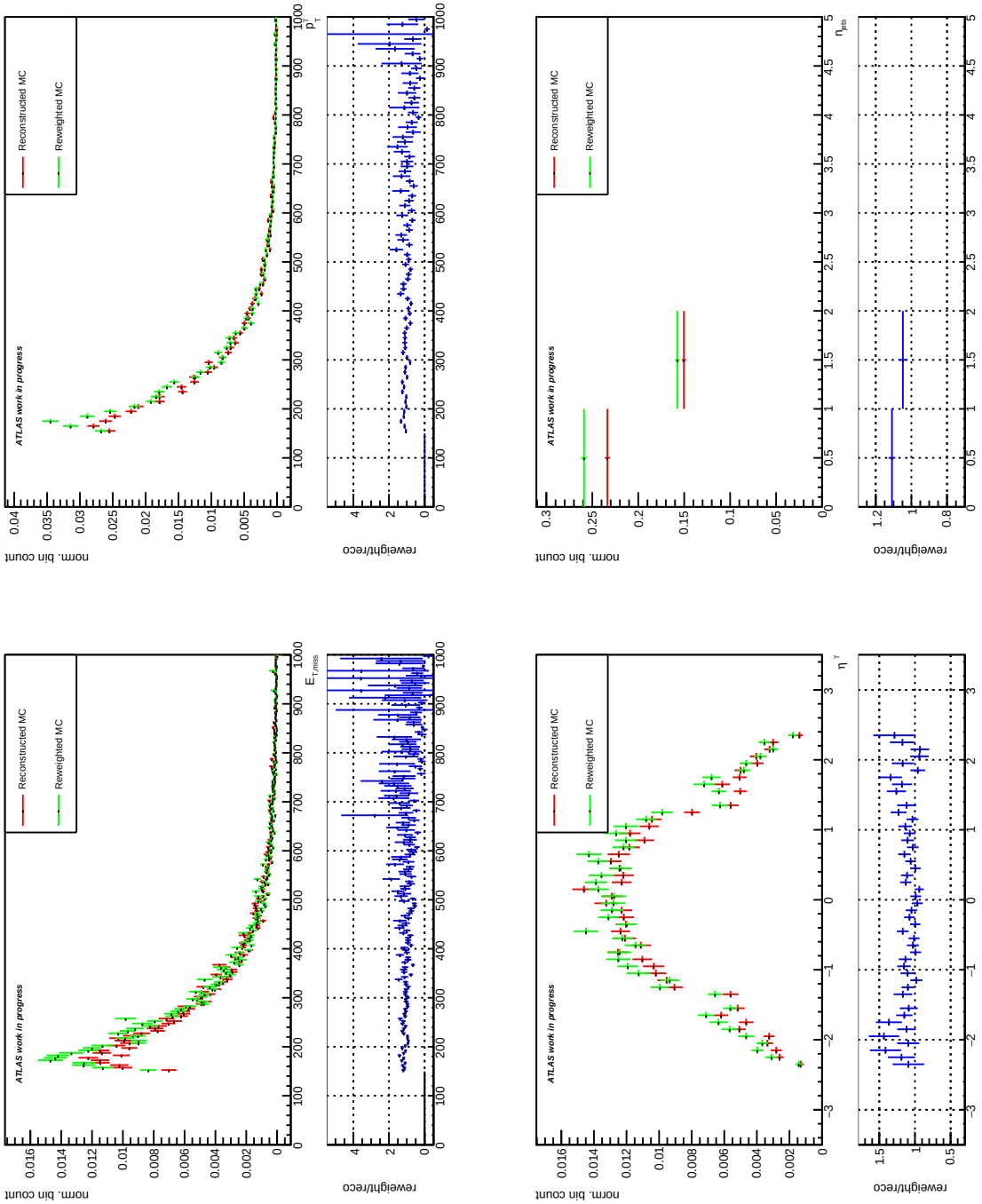

Figure 16: Comparison of kinematic distributions obtained from reconstruction and from reweighting, as described in section 9. The base model ($M_{med} = 1100$GeV, $m_\chi = 10$GeV) and the target model ($M_{med} = 1200$GeV, $m_\chi = 10$GeV) were used.

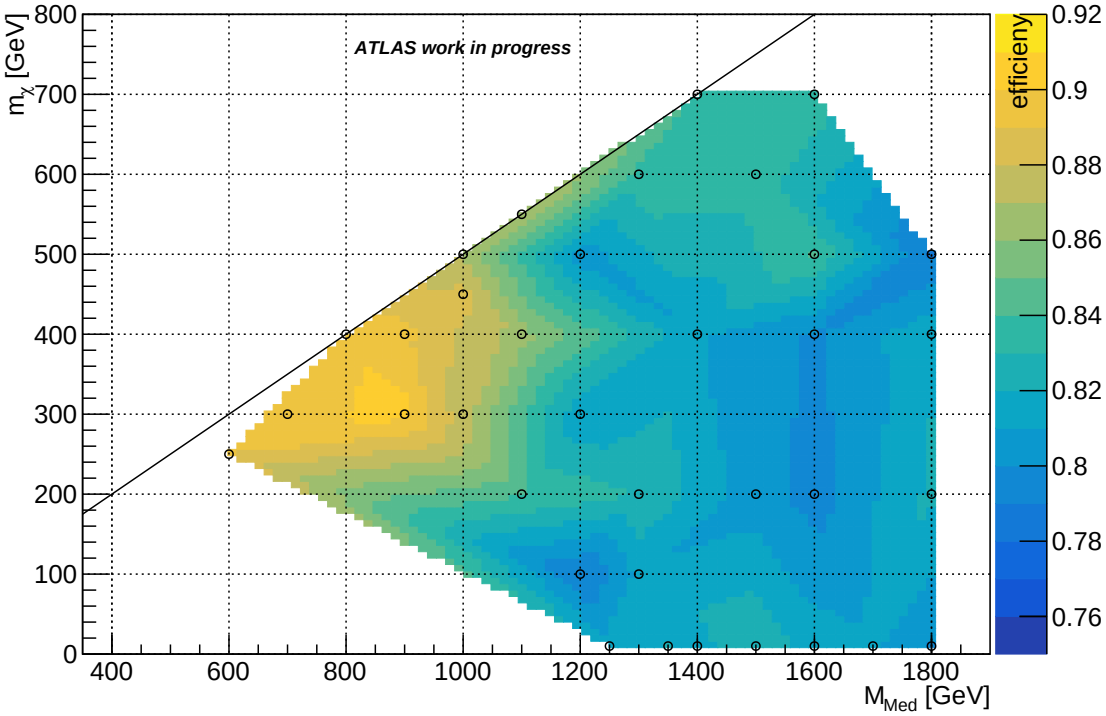

Figure 17: Efficiencies resulting from the reweighting method (section 9). The black dots represent the points of M_{med} and m_χ for which the samples were cut on to obtain these efficiencies.

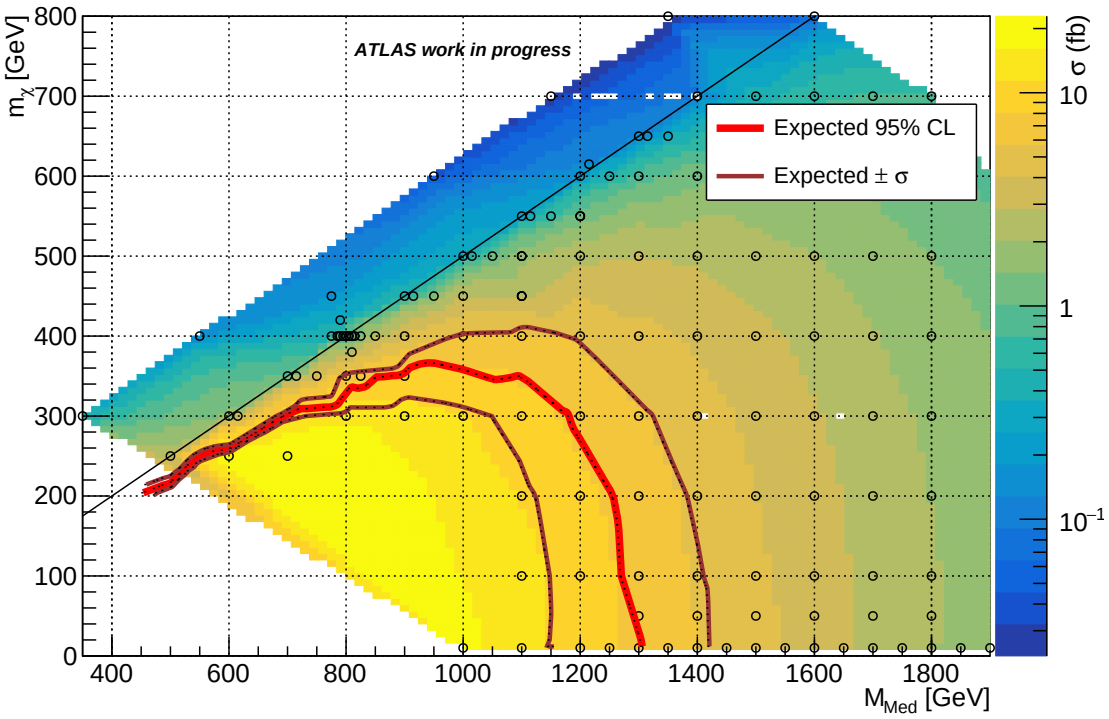

Figure 18: The cross section σ of the dark matter simplified model axial-vector interaction for varying parameters M_{med} and m_χ. The black circles represent the points that were explicitly tested. The exclusion line, obtained as explained in the text, resulting from this study which assumes $\mathcal{L}_{int} = 150 fb^{-1}$ is shown in red for comparison.

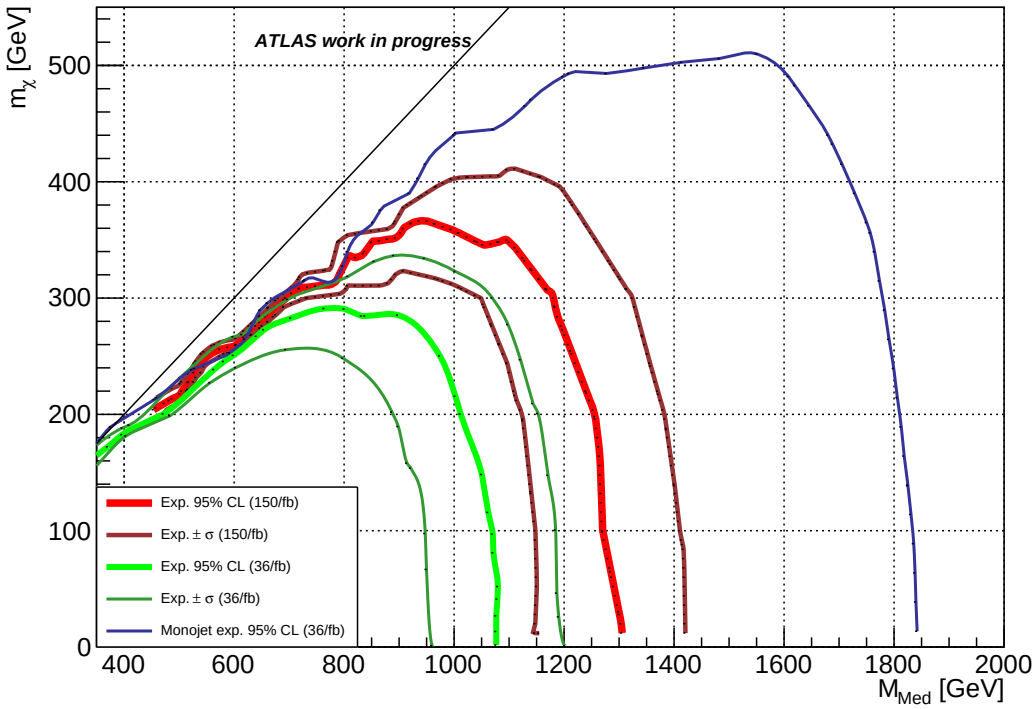

Figure 19: The exclusion line obtained in this study (red line), assuming a integrated luminosity of $\mathcal{L}_{int} = 150 fb^{-1}$. The line resulting from the 2017 analysis of the monophoton channel (ref) and the line from the monojet analysis (ref), which takes into account $\mathcal{L}_{int} = 36 fb^{-1}$, are shown for comparison.

Acknowledgments

I gratefully thank Fairouz Malek and Marie-Helene Genest from the LPSC Grenoble, who made this study possible. Their constant support, deep insights in the field of research and motivation were the basis for my work on this Bachelor thesis.

Erklärung

Ich versichere, dass ich diese Arbeit selbstständig verfasst und keine anderen als die angegebenen Quellen und Hilfsmittel benutzt habe.

Heidelberg, 27. September 2018, ...

Richard Naab